



**HAL**  
open science

## Preparation of nickel (oxide) nanoparticles confined in the secondary pore network of mesoporous scaffolds using melt infiltration

S. Chen, C. Ciotonea, A. Ungureanu, E. Dumitriu, C. Catrinescu, Robert Wojcieszak, F. Dumeignil, S. Royer

### ► To cite this version:

S. Chen, C. Ciotonea, A. Ungureanu, E. Dumitriu, C. Catrinescu, et al.. Preparation of nickel (oxide) nanoparticles confined in the secondary pore network of mesoporous scaffolds using melt infiltration. *Catalysis Today*, 2019, 334, pp.48-58. 10.1016/j.cattod.2019.01.064 . hal-02324307

**HAL Id: hal-02324307**

**<https://hal.science/hal-02324307>**

Submitted on 25 Oct 2021

**HAL** is a multi-disciplinary open access archive for the deposit and dissemination of scientific research documents, whether they are published or not. The documents may come from teaching and research institutions in France or abroad, or from public or private research centers.

L'archive ouverte pluridisciplinaire **HAL**, est destinée au dépôt et à la diffusion de documents scientifiques de niveau recherche, publiés ou non, émanant des établissements d'enseignement et de recherche français ou étrangers, des laboratoires publics ou privés.



Distributed under a Creative Commons Attribution - NonCommercial 4.0 International License

## **Preparation of nickel (oxide) nanoparticles confined in the secondary pore network of mesoporous scaffolds using melt infiltration**

S. Chen,<sup>a</sup> C. Ciotonea,<sup>a\*</sup> A. Ungureanu,<sup>b\*</sup> E. Dumitriu,<sup>b</sup> C. Catrinescu,<sup>b</sup> R. Wojcieszak,<sup>a</sup> F. Dumeignil,<sup>a</sup> S. Royer<sup>a</sup>

<sup>a</sup>Univ. Lille, CNRS, ENSCL, Centrale Lille, Univ. Artois, UMR 8181 - UCCS - Unité de Catalyse et Chimie du Solide, F-59000 Lille, France

<sup>b</sup>"Gheorghe Asachi" Technical University of Iasi, Faculty of Chemical Engineering and Environmental Protection, 73 Prof. D. Mangeron Blvd., 700050 Iasi, Romania

Corresponding authors: Dr. C. Ciotonea ([carmen.ciotonea@univ-lille.fr](mailto:carmen.ciotonea@univ-lille.fr)); Dr. A. Ungureanu ([aungureanu@tuiasi.ro](mailto:aungureanu@tuiasi.ro))

### **ABSTRACT**

Effective encapsulation strategies are highly sought-after in heterogeneous catalysis for preparing highly active and stable metal (oxide) nanocatalysts. Herein, we report an optimized Melt Infiltration (MI) procedure to confine nickel-oxide nanoparticles (NPs) into hierarchical microporous-mesoporous scaffolds. Three SBA-15 silica were synthesized in order to obtain different degrees of interconnectivity between the main mesopores. The impact of the SBA-15 pore characteristics, *i.e.*, this interconnectivity, also named secondary intra-wall porosity (IWP), on the final nickel (oxide) NPs size and localization has been specifically investigated. Using MI, which consisted in the diffusion of the precursor in the liquid state inside the porosity of the support in the presence of the native surfactant occluding the pores, selective localization of the NiO NPs inside the IWP was obtained, without large NPs plugging the main mesopores if IWP pores connecting the main mesopores do exist. When IWP – selective localization – occurs for the NPs, they show a size directly depending on the IWP dimensions. The obtained materials were tested, after reduction, in the hydrogenation reactions of cinnamaldehyde and 5-hydroxymethylfurfural. The as-obtained results underline the positive effect of

IWP - confinement of NPs to keep/maintain an elevated dispersion of the metallic Ni active phase and to reach a high catalytic activity in hydrogenation under mild reaction conditions.

**Keywords:** nickel; melt infiltration; nanoparticles; selective hydrogenation; biomass; mesoporous materials; heterogeneous catalysis

## 1. INTRODUCTION

Transition metals (TM) - based catalysts (*e.g.*, TM = Ni, Co, Fe, Cu) have a wide range of catalytic applications implying reactions such as hydrogenation, hydrogenolysis, hydrodeoxygenation, various energy transformation processes: Fischer–Tropsch synthesis, reforming, and water–gas shift reactions [1, 2, 3]. Hydrogenation reactions are of particular interest, considering the economic importance of the as-produced chemicals, including pharmaceuticals, agrochemicals, fragrances and flavors, intermediates, and other value-added products, for instance those derived from biomass. Consequently, TM-based catalysts were extensively studied during the last decades, with a specific focus on the preparation of highly dispersed and stable nanoparticles (NPs) supported on high-surface area materials in order to maximize the catalytic activity and/or selectivity as well as the long-term stability under reaction conditions [4].

To tailor the morphostructural properties and stability of transition metal (oxides) - TM(O) NPs in order to suit specific applications is however a difficult task, especially at high metal loading (> 5 wt.%), due to the mechanistically-complex NP growth by migration and coalescence, and Ostwald ripening during high-temperature catalyst activation and/or operation, resulting in a partial or even total loss of active surface [5, 6]. It was shown that the stability of NPs basically depends on (i) the properties of individual NPs (*i.e.*, particle size-dependent Tamman/Hüttig temperature and chemical composition), (ii) the properties of host structure (*i.e.*, pore architecture, surface area, surface properties), and (iii) the properties of particle/host system (*i.e.*, loading, spatial distribution of NPs, and strength of interactions between the support and NPs) [7, 8]. Therefore, there is still a strong motivation to improve the catalytic performance and stability of supported TM-based catalysts, to

meet the durability targets required for practical applications, which now calls for the design of active and stable NPs dispersed within mesoporous scaffolds.

Indeed, mesoporous materials encompassing members of silica SBA, KIT, MCM, FDU and MSU families have received much attention as prospective host structures for the guest NPs due to their unique structural, textural and chemical characteristics: high-surface area, controlled pore architecture, tunable pore size, adjustable chemical composition and so on [9-13]. There is a large diversity of methods for the preparation of supported TM(O) NPs into the porosity of mesoporous silica supports (*e.g.*, impregnation, sol-gel processes, sonochemical methods, deposition-precipitation or chemical vapor deposition), but impregnation (wet impregnation – WI, and incipient wetness impregnation – IWI) is by far the most used method [6]. Impregnation involves several successive steps [7]: (*i*) putting into contact the support with the solution of metal precursors such as nitrates, chlorides and acetates; (*ii*) maturation and solvent evaporation by drying of the impregnate, (*iii*) thermal decomposition of the precursor and stabilization of the material, and (*iv*) activation of the catalyst for the specific application. Each step has to be carefully optimized (concentration of precursor in the initial impregnation solution, temperature and time of drying, heating rate and gas atmosphere for the stabilization/activation, etc.); It is noteworthy that the drying step is particularly important in order to reach a homogeneous repartition of NPs throughout the support surface [14]. On the contrary, thermal stability of emerged NPs is mostly conditioned by the interactions between the support surface and the dispersed active phase [15, 16].

One of the most efficient and direct approaches to improve thermal stability of catalysts is to encapsulate (confine) the active metal (oxide) NPs inside the pore channels of the mesoporous scaffolds to mitigate particle growth [3, 4]. By this way, the mesoporous materials act as: (*i*) physical shields to prevent the coalescence of NPs, (*ii*) nanoreactors to spatially confine NPs and suppress their growth, or (*iii*) modulators of metal (oxide)-support interactions to suppress sintering. Such encapsulated catalysts are renowned as superior catalytic systems regarding their catalytic activity, selectivity and reusability. We previously applied this approach to produce sintering-resistant materials obtained by confining NPs in the main mesopores of ordered SBA-15, using IWI approach [14, 17].

However, by confining NPs in mesopores: (i) relatively large NPs are obtained, having a size close to the mesopore diameter (~8 nm in the case of SBA-15), and (ii) some pore plugging occurs, that could result in inaccessible catalytic centers, decreased activity, and significant mass-transfer resistances.

Less often used for the preparation of TM(O) NPs encapsulated inside the pores of mesoporous supports is the Melt Infiltration (MI) method [18]. MI consists in blending the support and the precursor in solid form, followed by a calcination of the mixture [18, 19]. As compared with the impregnation methods, MI solves some drawbacks related to the diffusion of precursor solution during the impregnation step and/or the drying step [20-24], while it is a solvent-free, green synthesis procedure. The control of the final dispersion for MI-derived materials can be achieved by changing several parameters such as the nature and structure of the support and the time of infiltration applied prior to the calcination step [25]. Ordered mesoporous silica scaffolds were generally used as supports for MI preparation (MCM-41, KIT-6, SBA-15), based on their high surface areas and abundant surface silanol groups, which favor an improved wettability of the support by the molten phase [26-29]. Nevertheless, TM(O) NPs with sizes close to that of the support pores' diameter are usually reported, meaning confinement of NPs in the main mesopores [30-32]. A significant improvement for the dispersion of the TM(O) NPs was observed when SBA-15 support pores are occluded with the porogen surfactant molecules. For instance, we recently reported an optimized MI method (MI-IWP, Melt Infiltration in the Intra-Wall Pores), which led to small NPs (< 2 nm) encapsulated inside the secondary pore network of SBA-15 showing an excellent thermal stability up to 900 °C (oxidizing/reducing atmospheres), whereas the main mesopores remained fully opened and free of bulky NPs [25, 26].

One of the remarkable properties of the SBA-15-type support is the hierarchical microporous-mesoporous architecture and the possibility to control the secondary porosity (*i.e.*, the intra-wall porosity – IWP; generated by removal of wall-inserted ethyleneoxide segments of the P123 surfactant molecule), simply by the hydrothermal (ageing) temperature or using swelling agents [33-37]. Playing on the temperature of ageing is particularly an effective way to change the secondary porosity from ultramicroporosity (pore size < 1 nm) to secondary mesoporosity [33-36] as well as the degree of pore

interconnectivity. The IWP can significantly contribute to the total pore volume of the host material and provide a unique, yet incompletely explored confinement space for encapsulating NPs at a very small size. We investigate herein the impact of the secondary porosity on the infiltration efficiency of nickel precursor-based molten phase in the pores of SBA-15 occluded with Pluronic P123 surfactant. In principle, interconnected micro-mesoporous channels in SBA-15 should facilitate mass-transfer of melted precursors to the support internal surface during MI preparation, which is crucial to achieve small and stable NPs encapsulated within the secondary pores of the mesoporous scaffold. Effect of this secondary porosity consisted in: (i) it determined the final dispersion of the nickel active phase, (ii) its thermal resistance to sintering, and (iii) the catalytic properties for hydrogenation reactions. The study shows that the interconnected mesochannel network provides spaces for direct access of guest nickel precursor species, and suppress the growth of particles during the thermal steps, while preventing as well significant blockage of the main mesopores with confined NPs.

## **2. EXPERIMENTAL PROCEDURES**

### **2.1. Chemicals**

All chemicals required to synthesized mesoporous SBA-15 silica and Ni-containing catalysts were used as purchased: tetraethylorthosilicate ( $\text{Si}(\text{OC}_2\text{H}_5)_4$ , TEOS, 98%, Sigma-Aldrich), non-ionic triblock copolymer Pluronic P123 (poly(ethyleneoxide)-block-poly(propyleneoxide)-block-poly(ethyleneoxide)-block),  $\text{PEO}_{20}\text{PPO}_{70}\text{PEO}_{20}$ , molecular weight of 5800, BASF Corp.), hydrochloric acid (HCl, 37%, Sigma-Aldrich), hexahydrate nickel nitrate ( $\text{Ni}(\text{NO}_3)_2 \cdot 6\text{H}_2\text{O}$ , 98%, Sigma-Aldrich).

Chemicals used for the hydrogenation reactions were also used as received: trans-cinnamaldehyde ( $\text{C}_6\text{H}_5\text{-CH=CH-CHO}$ , 98%, Merck) as reagent and *iso*-propanol ( $\text{C}_3\text{H}_8\text{O}$ , 99%, Sigma-Aldrich) as solvent, 5-hydroxymethylfurfural (HMF, 99%, Sigma-Aldrich) as reagent and 1,4-dioxane (99.8 %, Sigma-Aldrich) as solvent.

### **2.2. Material synthesis**

2.2.1. *Support syntheses:* Three SBA-15 supports were synthesized according to classical procedure [37], and changing the ageing temperature to reach different secondary porosity properties [33, 34]. 4 g of Pluronic P123 were dissolved in a 1.6M solution of HCl at 40 °C. Thereafter, 8.5 g of a TEOS, was added dropwise to the solution, and the solution was submitted to magnetic stirring for 24 h. The resulting gel was submitted for 48 h to hydrothermal ageing, at 60 °C, 100 °C or 140 °C. After recovering by filtration, the SBA-15 samples were washed with water, and dried at 100 °C for 24h. *The dried SBA-15 samples were the materials used for the melt infiltration procedure.* However, for characterization purpose, parts of the different supports were calcined at 550 °C for 6 h in a muffle furnace, using a heating ramp of 1.5 °C min<sup>-1</sup>. *The calcined supports were named SBA-15\_T, where T (ageing temperature in °C) = 60, 100 and 140.*

2.2.2. *Nickel catalyst preparation:* an adequate mass of Ni(NO<sub>3</sub>)<sub>2</sub>·6H<sub>2</sub>O precursor (calculated to obtain 10 wt.% of Ni in the final material) was first hand mixed with selected dried SBA-15 support. Following the method reported in our previous studies [25, 26], the mixture was heat-treated at 57 °C for 4 days (optimized diffusion time as reported in [25]). Once the diffusion step was completed, the solid was calcined under static conditions at 500 °C for 5 h, using a heating rate of 1.5 °C min<sup>-1</sup>. *The calcined materials, NiO/SBA-15 samples prepared on the different supports, were named Ni\_T, where T = 60, 100 and 140 (the temperature in °C at which the support was aged).*

### 2.3. Material characterization

The chemical composition of the samples was determined by ICP analyses using sequential scanning inductively coupled plasma with an optical emission spectrometer (Perkin Elmer Optima 2000 DV). A known amount of sample was dissolved in a diluted HF-HCl solution and heated under microwave until complete dissolution. Results showed that the Ni final loading was in agreement with the expected 10 wt.% ± 0.3 wt.%.

X-ray diffraction patterns were recorded on a PANalytical Empyrean X-ray diffractometer in Bragg-Brentano configuration, with a CuK $\alpha$  radiation ( $\lambda = 1.54184 \text{ \AA}$ ). For small-angle

analysis, the data were collected in a  $2\theta$  range from  $0.5$  to  $5^\circ$  with a step size of  $0.01$  each  $2s$ . Wide-angle analyses were performed using a  $2\theta$  range between  $10$  and  $80^\circ$  with a step size of  $0.05^\circ$  each  $2s$ . Crystal average size was calculated using the Scherrer equation:  $D_{hkl} = K\lambda/b\cos\theta$ , where  $K$  is a structure constant ( $0.9$  for spherical crystals);  $\lambda$  is the incident ray wavelength;  $b$  is the peak width at half height after correction for instrumental broadening; and  $\theta$  is the Bragg angle.

$N_2$  physisorption experiments were performed at  $196^\circ\text{C}$ , on a Micromeritics Tristar II Plus instrument. Before analysis, a known mass of  $\sim 0$  mg of solid was heat-treated under vacuum at  $350^\circ\text{C}$  for  $3$  h. Specific surface area ( $S_{BET}$ ) was calculated using the B.E.T. equation, on the linear part of the B.E.T. plot ( $P/P_0=0.10-0.25$ ) of the desorption branch. Pore volume ( $V_p$ ) was measured on the adsorption branch of the isotherms, at a  $P/P_0$  value of  $0.98$ . The  $t$ -plot method was applied to quantify the micropore volume and surface area (de Boer statistical thickness of  $3.8-6.5$  Å). Pore diameter ( $D_p$ ) was calculated applying the Barrett-Joyner-Halenda model on the desorption branch of the isotherms. Cumulative pore volume was calculated on the desorption branch of the isotherms, using the non-local density functional theory (NL-DFT) model for silica cylindrical pores (equilibrium model).

Samples were analysed by transmission electron microscopy (TEM, JEOL 2100 UHR, operated at  $200$  kV with a  $\text{LaB}_6$  source and equipped with a Gatan Ultra scan camera). Samples were embedded in a polymeric resin (spurr), before being sliced into  $50$  nm-thick sections using an ultramicrotome, before being deposited on a carbon grid.

Temperature-programmed reduction under  $H_2$  ( $H_2$ -TPR) was conducted on an AUTOCHEM chemisorption instrument (Micromeritics) equipped with a TCD. Before  $H_2$ -TPR experiment, the catalyst was activated up to  $500^\circ\text{C}$  (heating ramp of  $10^\circ\text{C}\cdot\text{min}^{-1}$ , plateau of  $1$  h) under simulated air (total flow rate of  $50$   $\text{mL}\cdot\text{min}^{-1}$ ). After cooling down to  $50^\circ\text{C}$ , the  $H_2$ -containing flow was stabilized ( $50$   $\text{mL}\cdot\text{min}^{-1}$ ,  $5.0$  Vol.%  $H_2$  in Ar) and the temperature-programmed reduction was performed (from  $50$  to  $900^\circ\text{C}$ , with a temperature ramp of  $5^\circ\text{C}\cdot\text{min}^{-1}$ ).

#### **2.4. Catalytic hydrogenation reactions**

Catalytic performances of Ni/SBA-15 materials were first assessed in the high-pressure hydrogenation of cinnamaldehyde reaction. Calcined NiO/SBA-15 precursors (Ni\_T samples), were reduced at 500 °C for 10 h (heating ramp of 6 °C.min<sup>-1</sup>) under H<sub>2</sub> flow (1 L.h<sup>-1</sup>). After this reduction step, the reaction was performed in a Parr reactor under the following typical conditions: 1 mL cinnamaldehyde, 40 mL *isopropanol* as a solvent, 0.133 g catalyst, 10 bar H<sub>2</sub> and reaction temperature of 60 °C. Preliminary tests were performed with different granulometric fractions, stirring rates and catalyst loadings, to determine conditions under which no diffusional limitations will occur: grain size lower than 0.126 mm, stirring rate of 750 rpm, 0.066-0.265 g catalyst. In addition, a blank experiment was conducted under N<sub>2</sub> pressure (instead of H<sub>2</sub>), in order to confirm the absence of hydrogenation product by hydrogen-transfer reaction (after 6 h of reaction). Finally, a blank experiment with calcined SBA-15\_100 sample was performed to determine the support impact on the cinnamaldehyde concentration in solution. No modification of the concentration is observed after 6 h of reaction. Aliquots of the reaction mixture were withdrawn periodically and analyzed by gas chromatography (HP 5890, equipped with a DB-5 capillary column and a FID detector). The identification of the reaction products was achieved from the retention times of pure compounds and from additional analysis by GC-MS (Agilent 6890 N, equipped with an Agilent 5973 MSD detector and a DB-5-ms column).

The hydrogenation reaction of 5-hydroxymethylfurfural (HMF) was performed in a SPR multi-reactor (6 mL total volume) from Unchainedlabs. Prior to the catalytic tests, the catalysts were reduced at 550 °C for 2 h (heating ramp of 10 °C.min<sup>-1</sup>) under 5 Vol.% H<sub>2</sub> in Ar flow (50 mL.min<sup>-1</sup>). For a typical reaction, the reactor was charged under the controlled atmosphere of a glove box with 0.030 g of HMF, 1.5 mL of *1,4-dioxane* as a solvent and 0.021 g of catalyst, sealed and purged with H<sub>2</sub>. Then, the reactor was pressurized with 15 bar H<sub>2</sub>, heated at 130 °C and stirred at a speed of 700 rpm for 1 h. Blank experiment, performed with calcined SBA-15\_100 showed 1.5 mol.% conversion of HMF. This conversion could be most probably associated to an adsorption of HMF on the support surface. The products were collected and analyzed by GC (Shimadzu 2010 Plus) equipped with ZB-WAX Plus capillary column (30.0 m × 0.25 mm × 0.25 μm) and a flame ionization detector (FID), and by GC-

MS (Shimadzu QP2010 Ultra EI) equipped with a ZB-1XT capillary column (15.0 m × 0.53 mm × 0.25 μm) and a FID detector.

### 3. RESULTS AND DISCUSSION

#### 3.1. Pore structure periodicity in SBA-15 supports and NiO/SBA-15 materials

The low angle XRD patterns registered for the SBA-15\_T calcined supports are presented in Figure 1. The three support diffractograms show the main peaks associated to the (100), (110) and (200) lattice reflections of the ordered hexagonal pore structure with  $P6mm$  symmetry. The presence of the three reflections indicates a good mesostructure ordering for the three supports [38-40]. The presence of (210) and (300) reflections at  $2\theta > 2^\circ$ , for materials synthesized at ageing temperature above 100 °C, are evidences of an excellent textural uniformity in SBA-15\_100 and SBA-15\_140. The evolution of the mesostructure geometric characteristics is directly reflected by the changes in the reflection positions (modification of interplanar spacing, “ $d$ ” and cell parameter, “ $a$ ”, with modification of wall thickness and main mesopore diameter).

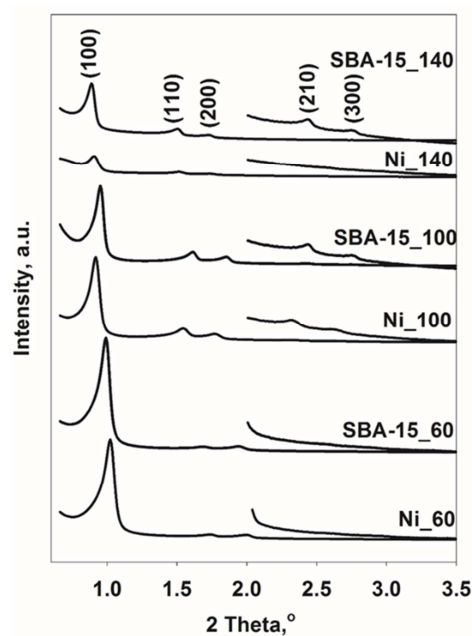


**Figure 1.** Low-angle XRD patterns recorded for SBA-15\_T supports and Ni\_T materials in calcined forms.

When ageing temperature is increased from 60 °C to 140 °C, (100) reflection shifted at lower  $2\theta$ , given a cell parameter increasing from 10.2 nm to 11.4 nm (Table 1). This increase in cell parameter is mostly issued from the P123 micelle size dilatation with the temperature of ageing [33]. After deposition of the nickel oxide phase (Ni\_T samples), only few modifications of the diffractograms are visible (Figure 1). As a first remark, the remaining of the three major reflections confirms the maintaining of the pore ordering after melt infiltration procedure and further decomposition of the precursors to form NiO. A decrease in the reflection intensities is observed, which could be explained by the specific localization of the NiO NPs inside the support pores that become filled, thus reducing the electron density contrast between the pores and silica walls [17]. Very small changes in  $d(100)$  spacing (Figure 1) and cell parameter values ( $a_0$ , Table 1) are also measured between calcined support and calcined NiO materials. A  $\pm 0.3$  nm fluctuation of the  $a_0$  values is then measured. This result suggests no significant modification of the hexagonal cell when the MI procedure is performed, and that the materials prepared by the MI process possess comparable properties than those of the pure SBA-15 supports synthesized under the different ageing conditions. The limited variation in  $a_0$  is not associated to the shrinking of the mesopores in the materials, and is preferably associated to the deposition of the nickel phase inside the mesopores, inducing a modification of the scattering contrast between the SBA-15 walls and the material deposited in the pores and reported to be at the origin of (i) the variation of the intensity of the (100) reflection as previously mentioned, and (ii) small  $a_0$  values variations [17].

### **3.2. Textural properties of SBA-15 supports and evolutions in NiO/SBA-15 materials**

The textural properties issued from nitrogen physisorption experiments are gathered in Table 1, while the isotherms are presented in Figure 2. For all samples, N<sub>2</sub> adsorption-desorption isotherms of supports, as well as of NiO/SBA-15 catalyst precursors (Ni\_T materials), are of type IV (Figures 2). Type IV is characterized by a plateau of saturation, and is obtained over mesoporous materials in which capillary condensation occurs within the pores. The length of the plateau of saturation is significantly affected by the ageing temperature applied to obtain the support, being the longest for SBA-15\_60 and being almost not visible for SBA-15\_140. This evolution indicates a significant

change in the pore diameter, as it can be confirmed following the evolution of the B.J.H. pore diameter (Table 1), observed to increase from 5.4 nm (SBA-15\_60) to 14.0 nm (SBA-15\_140). Comparing these values obtained over the supports with those obtained for Ni\_T materials, it appears that the MI process has very limited effect on the main mesopore size, confirming data issued from low-angle XRD. A hysteresis forms between the adsorption and the desorption branches of the isotherms, which is of H1-type (parallel and vertical adsorption and desorption branches, Figure 2). These characteristics fit perfectly with the expected SBA-15 textural properties. Consequently, after MI process and further calcination for supported NiO formation, the supports retain their excellent ordering degrees, whatever the ageing temperature used (60 °C, 100 °C or 140 °C).

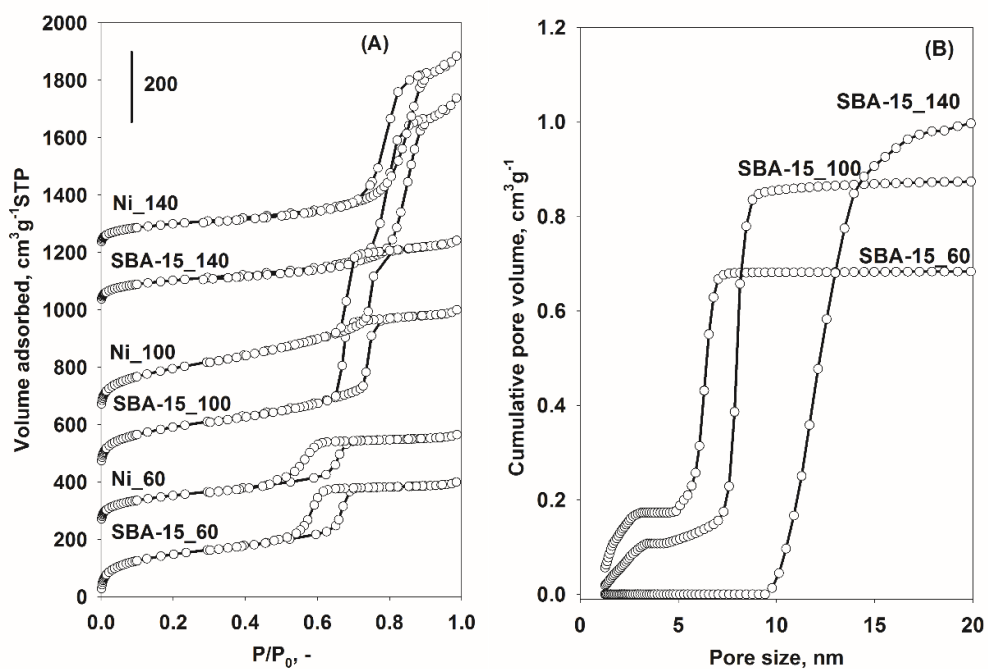


**Figure 2.** (A) N<sub>2</sub> physisorption isotherms recorded for SBA-15\_T supports and Ni\_T materials in calcined forms. For sake of clarity, isotherms are shifted by 200 cm<sup>3</sup> g<sup>-1</sup> each; (B) NL-DFT cumulative pore volume as a function of the pore diameter recorded for the supports in the calcined forms.

Table 1. Textural and structural properties of the synthesized materials.

Sample	$S_{BET}^a$	$S_{\mu}^b$	$V_p^c$	$V_{\mu}^d$	$D_p^e$	$a_0^f$	$d_{NiO} / \text{nm}$
	m <sup>2</sup> .g <sup>-1</sup>	m <sup>2</sup> .g <sup>-1</sup>	cm <sup>3</sup> .g <sup>-1</sup>	cm <sup>3</sup> .g <sup>-1</sup>	nm	nm	XRD TEM

SBA-15_60	765	291	0.71	0.128	5.4	11.4	-	-
Ni_60	537	168	0.55	0.074	5.4	11.1	8.5	n.a.
SBA-15_100	673	116	0.91	0.050	6.8	10.6	-	-
Ni_100	498	34	0.83	0.013	6.6	10.9	n.d.	2.1
SBA-15_140	361	68	1.10	0.030	14.0	10.2	-	-
Ni_140	350	64	1.02	0.027	13.7	9.9	3.5	3,1

<sup>a</sup>, B.E.T. surface area; <sup>b</sup>, microporous surface area; <sup>c</sup>, total pore volume; <sup>d</sup>, micropore volume; <sup>e</sup>, B.J.H. mean pore size; <sup>f</sup>, unit cell parameter; n.d.: not detectable; n.a.: not applicable.

Besides the pore diameter, B.E.T. surface area, microporous surface area, and total pore volume are also significantly affected by the ageing temperature (Table 1). As can be expected together with a pore diameter increase (when the ageing temperature increases), the pore volume increases (from 0.71 cm<sup>3</sup>.g<sup>-1</sup> to 1.10 cm<sup>3</sup>.g<sup>-1</sup>), while the surface area decreases (from 765 m<sup>2</sup>/g to 361 m<sup>2</sup>/g). At the same time, some fluctuations of the microporous characteristics of the materials are observed, reflecting the changes in the properties of the secondary porosity. Comparison of textural properties obtained in this work is paralleled to observations done in references dealing with pore topology of SBA-15 with synthesis temperature [33, 34], with at low temperature of ageing (60°C in this study), a significant proportion of micropore forms, with a  $S_{\mu}$  of 291 m<sup>2</sup>/g and a  $V_{\mu}$  of 0.128 cm<sup>3</sup>/g obtained. At this ageing temperature, it was previously reported that SBA-15 presents small mesopores and thick walls (comparable to the distance consecutive hydrated micelles in water, ~ 4 nm) and ultramicropores, as well [41, 42]. As the silica walls may replicate the topology of the hydration shells of the PEO chains in water, at temperature of ageing of 60 °C, no micropores bridging the main mesopores are expected [33]. The presence of such low size porosity is visible on the cumulative pore volume evolution with pore size for the SBA\_60 sample (Figure 2(B)) that is the support presenting the largest volume associated to pores of low size, and the smallest main mesopore size. After ageing at 100 °C, P123 mesophase is modified since the temperature exceeds the cloud point of the surfactant (~90 °C) [43]. Under such conditions, a decrease in the strength of the interaction between the surfactant and the inorganic matter results in the densification of the walls, which is reflected in the

final material by the formation of larger mesopores and thinner silica walls, as observed in this study for the SBA-15\_100 (Table 1). The presence of a secondary porosity is the result of the collapse of the ultramicropores (decreases in  $S_{\mu}$  and  $V_{\mu}$ , Table 1). In this case, micropores and small mesopores connecting the adjacent mesopores are expected, with sizes in the range of 1.5-4 nm [33, 34], such pores contributing to the cumulative pore volume of the support in Figure 2(B) for this sample. Compared to the properties of the SBA-15\_60, a decrease of the micropore fraction, as well as an increase of the main mesopore size are easily observed over SBA-15\_100 in Figure 2(B). Finally, when the ageing temperature is increased at 140 °C, the destabilization of the corona of PEO due to the loss of hydration  $H_2O$  at high temperature resulted in a decreased micelle surface / silica interaction [43]. As described in the literature, densification of the silica walls will occur to bring about an important decrease in the wall thickness and microporous volume. Therefore, compared to the material synthesized at 100°C, the SBA-15\_140 presents larger mesopores (14.0 nm), separated by 2 nm - width silica walls, and being crossed by a secondary mesoporosity according to the pore topology model given in [33]. In our case, applying the NL-DFT model to the desorption branch did not allow to detect such secondary bridging mesoporosity (even if residual micropore volume is detected applying t-plot method, Table 1), and only a pore volume associated to the main mesopores is visible in Figure 2(B). However, the reduced width of the hysteresis loop supports the formation of fully interconnected 3-D network of mesochannels [34]. Such hysteresis behavior is consistent with that observed for KIT-6 materials with interconnected 3-D pore network. After MI process, the NiO - containing materials exhibit slightly different textural properties. The most important differences are noticed between SBA-15\_60 and Ni\_60, with decreases of  $S_{BET}$  (-30%) and  $V_p$  (-22%), associated with important decreases in microporous surface area (-42%) and volume (-42%). In the case of the Ni\_100 and Ni\_140 samples, the variations of surface area and pore volume are lower. Only an important decrease of the microporous surface is measured between SBA-15\_100 and Ni\_100, of around 43 % (Table 1).

### 3.3. Support morphology, localization and size of NiO NPs

TEM images for the calcined forms of the MI-derived materials (Ni\_T materials) are presented in Figures 3-5. For the three materials, the SBA-15 pore topology is easily observed at low magnification. At high magnification, the changes in pore diameter and wall width with the ageing temperature are clearly observed. Thus, thick walls are observed at low ageing temperature, but wall thickness decreases with the temperature of ageing. Likewise, a progressive increase in pore diameter can be noticed.

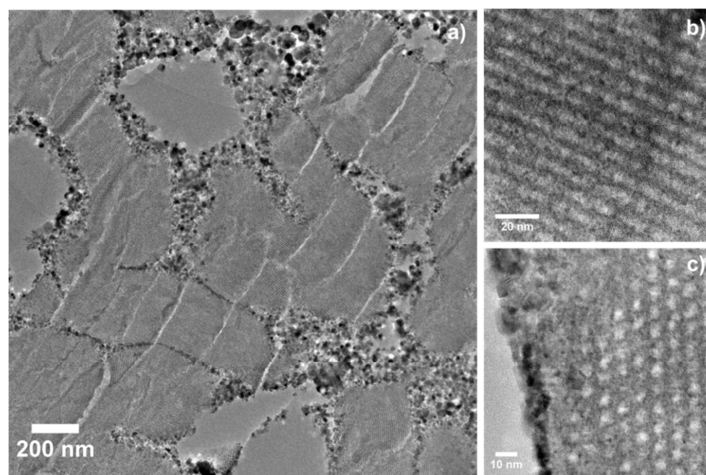


**Figure 3.** Selected TEM images obtained for Ni<sub>60</sub> material in calcined form: a) low magnification image; b) longitudinal view of the channels at high magnification; c) transversal view of the channels at high magnification.

Representative micrographs obtained for Ni<sub>60</sub> are presented in Figure 3. From Figure 3a, it is evident that most of the NiO NPs appear located around the silica grains, under the form of large aggregates of small particles. Analysis of the images allows to plot the particle size histogram (Figure 6a). Elementary particles constituting the external aggregates are of wide size, most of them being above 10 nm. High magnification observation on the silica grain evidences the formation of some small NPs located inside the pores, with a size below 5 nm. However, the frequency of this low size particle population is approximately 15% (Figure 6a), meaning that most of the NiO are present as external phases. Consequently, these results show that the optimized melt infiltration does not allow to obtain fine NPs homogeneously dispersed inside the silica grains, when the SBA-15<sub>60</sub> support is used.

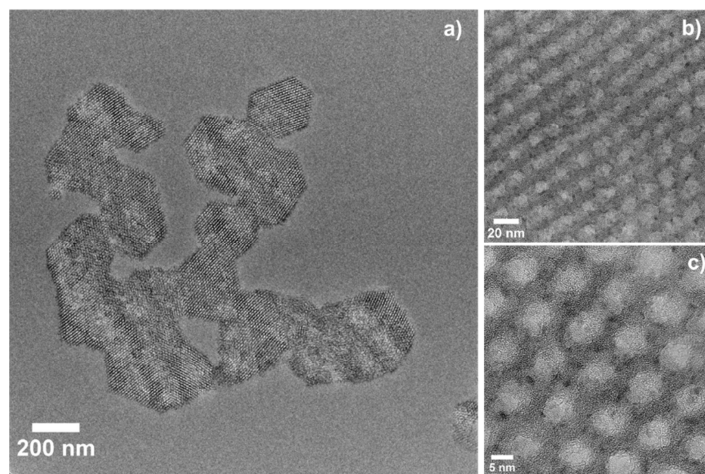


**Figure 4.** Selected TEM images for Ni<sub>100</sub> material in calcined form: a) low magnification image; b) longitudinal view of the channels at high magnification; c) transversal view of the channels at high magnification.

Low magnification images of the Ni<sub>100</sub> sample (Figure 4a) are completely different from those acquired on Ni<sub>60</sub>. Indeed, no extra-porous oxide phases can be detected, despite the similar nickel loading. Increasing the magnification allows distinguish the mesopores (Figure 4b) which are free of mesopore confined NPs (~10 nm in size), as usually observed when classical IWI or MI procedures are applied for the preparation [14, 15, 17, 25, 26]. Remarkably, the formation of very small NPs is observed, and they appear as located inside the silica wall (Figure 4b,c). Statistical analysis of images (Figure 6) showed that NiO particles are exclusively below 3nm in size, 90 % of them being of 2 nm (average size of 2.1 nm, Table 1). Consequently, for the support obtained at 100 °C, the optimized MI approach is highly efficient to encapsulate small NiO NPs inside the pores of SBA-15, with a very fine and homogeneous distribution over the mesoporous scaffold, in contrast with SBA-15<sub>60</sub>.

Finally, Figure 5 shows the results obtained for Ni<sub>140</sub>. Low magnification image (Figure 5a) and high magnification images (Figure 5b,c) evidenced a behavior comparable with Ni<sub>100</sub>: (i) absence of external NiO NPs formation, (ii) absence of ~10 nm mesopore confined NiO NPs plugging the pores, and (iii) formation of fine NPs with sizes largely below the main mesopore size and being relatively homogeneously distributed throughout the silica grains. Thus, the main difference between Ni<sub>140</sub> and Ni<sub>100</sub> resides in the size of the NPs produced, which are observed to be not monomodal (Figure 6c),

with an average size measured at 3.1 nm (Table 1). It can be concluded that, similarly with SBA-15\_100, the optimized MI approach is efficient to disperse NiO in SBA-15\_140 support, and that the particle size is essentially controlled by the intra-wall pore dimensions.

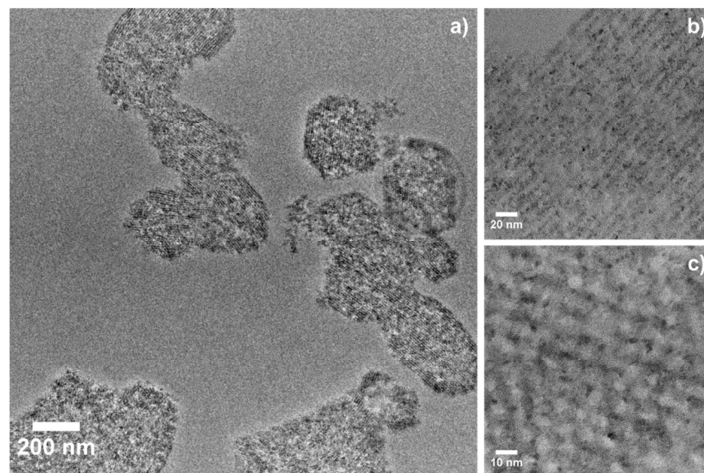


**Figure 5.** Selected TEM images for Ni\_140 material in calcined form: a) low magnification image; b) longitudinal view of the channels at high magnification; c) transversal view of the channels at high magnification.

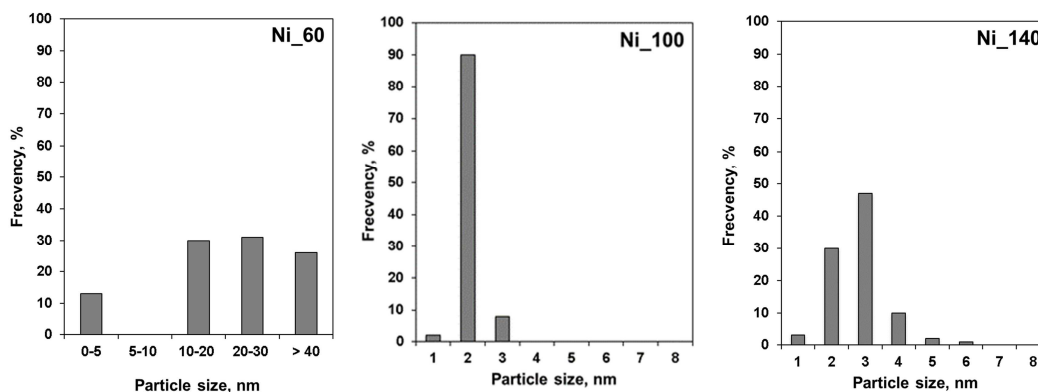


**Figure 6.** NiO Particle size distribution in Ni\_T materials in calcined forms.

These interesting results, clearly showing the lack of dispersion efficiency in the case of SBA-15\_60 and the difference in NiO NPs size obtained over SBA\_100 and SBA\_140 supports, can be rationalized by taking into consideration the different textural properties and pore architectures for the distinct SBA-15 host materials. Thus, SBA-15\_60 is the only support in the series showing not interconnected mesoporosity, and in this case, we observed that the diffusion of the molten precursor

is not efficient. Such problem is not encountered for the two other SBA-15 supports synthesized at higher ageing temperature, which display interconnected mesoporosity, and demonstrate an efficient and complete infiltration of the molten phase inside the pores of the scaffolds (Ni\_100 and Ni\_140, Figures 4 and 5). At the same time, as Ni\_140 is obtained over a support prepared at a higher ageing temperature than Ni\_100, the secondary pores increase in size, and evolves from microporous to small mesoporous. The evolution of the mean NiO NPs size shown in Figure 6 follows the trend in the size of secondary pores, which is a clear indication that NiO NPs are confined inside the intra-wall porosity of the mesoporous hosts. Diffractograms recorded over the different Ni\_T samples at wide-angles (Figure 7) are in agreement with TEM observations and reinforce this interpretation. Reflections ascribed to NiO are only distinguished for Ni\_60 and Ni\_140, whereas average NiO crystal domain sizes are of 8.5 nm and 3.5 nm (calculated by Scherrer equation), respectively. For Ni\_100, no crystalline NiO phases can be detected by XRD, yet some fluctuations in the pattern baseline are observed at positions corresponding to NiO, clearly demonstrating that NPs are highly dispersed, in line with the analyses by TEM (Figure 4).

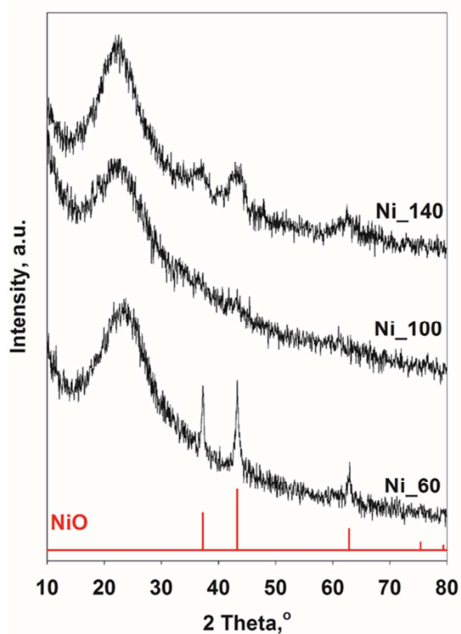


**Figure 7.** Wide-angle X-ray diffraction patterns obtained for Ni\_T materials in calcined forms. Bottom: NiO, JCPDS file n°47-1049.

### 3.4. Activation of the catalyst

Considering the hydrogenation applications, the reducibility of nickel oxide phase in the different materials was investigated by TPR (Figure 8). First, the hydrogen consumed during the TPR process was evaluated to correspond to the quantity necessary to fully reduce NiO into Ni<sup>0</sup> ( $\pm 5\%$  of the theoretical value). These data indicate the accessibility of the NiO NPs to hydrogen, even if they are located in the intra-wall pores of mesoporous silica scaffolds.

Reduction of NiO in Ni<sub>60</sub> occurs in two distinct steps: (1) first hydrogen consumption step centered at 308 °C; (2) second hydrogen consumption centered at 478 °C. For the two other materials, Ni-100 and Ni<sub>140</sub>, the first hydrogen consumption step is significantly depressed and most of the hydrogen consumption (> 90%) occurs during the second step with the reduction maximum at ~490 °C.

In the light of previous discussions concerning the size and distribution of NiO NPs, it seems reasonable to assume that:

- Reduction of bulk NiO, located at the external surface of the silica (observed only for Ni<sub>60</sub>), will occur at the lowest temperature,  $T_{max} \sim 310$  °C;
- Reduction of small size NiO particles, located in the intra-wall porosity of the mesoporous host, will occur at a higher temperature,  $T_{max} \sim 485$  °C [26, 43].

The presence of small broad hydrogen consumptions at  $T \sim 310$  °C for Ni<sub>100</sub> and Ni<sub>140</sub> suggests the presence of a very low fraction of NiO external particle of large size in these two materials, however not observed by TEM.

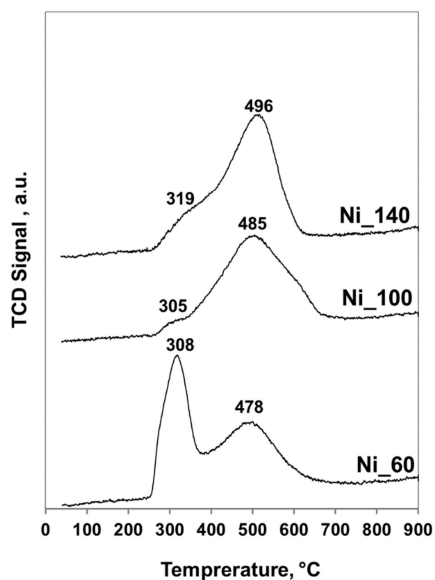


**Figure 8.** H<sub>2</sub> temperature programmed reduction profiles recorded for the Ni\_T materials in calcined forms.

Always in view of the practical application, stability of materials under reducing atmosphere was evaluated by TEM for Ni\_100 and Ni\_140 in order to determine if the produced NPs are thermally stable or suffer sintering during activation under hydrogen. Representative images are presented in Figure 9.

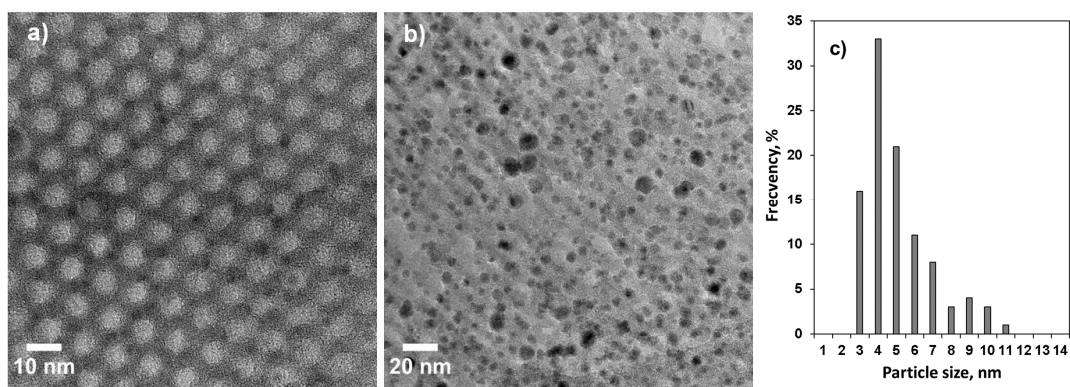


**Figure 9.** TEM images obtained for: a) Ni\_100 and b) Ni\_140 materials reduced *ex situ* at 900 °C. c) Particle size distribution for Ni\_140 after reduction at 900 °C.

For Ni\_100, no visible modification of the NPs size takes place upon activation under reducing conditions (Figure 9a). Observed Ni<sup>0</sup> NPs exhibit sizes always below or equal to 3 nm, very close to what was observed for the calcined form. This result supports our previous interpretation consisting in

a selective localization of the NPs inside the intra-wall pores of the support. A completely different behavior is obtained over Ni<sub>140</sub> materials. The corresponding material shows NPs of metallic Ni of larger size than the initial NiO NPs particle (Figure 9 b,c). Ni<sup>0</sup> NPs of size reaching 11 nm are observed, but the NPs population is centered at 4-5 nm, with an average NPs size calculated at 5.1 nm. Considering the textural features of the support synthesized at 140 °C, and the wall thickness, the silica walls are probably not robust enough upon this severe activation treatment, resulting in some alteration of the pore network periodicity (Figure 9b) and some visible – but remaining reasonable – Ni NPs sintering at high temperature (Figure 9c).

### 3.5. Catalytic properties of Ni/SBA-15 materials

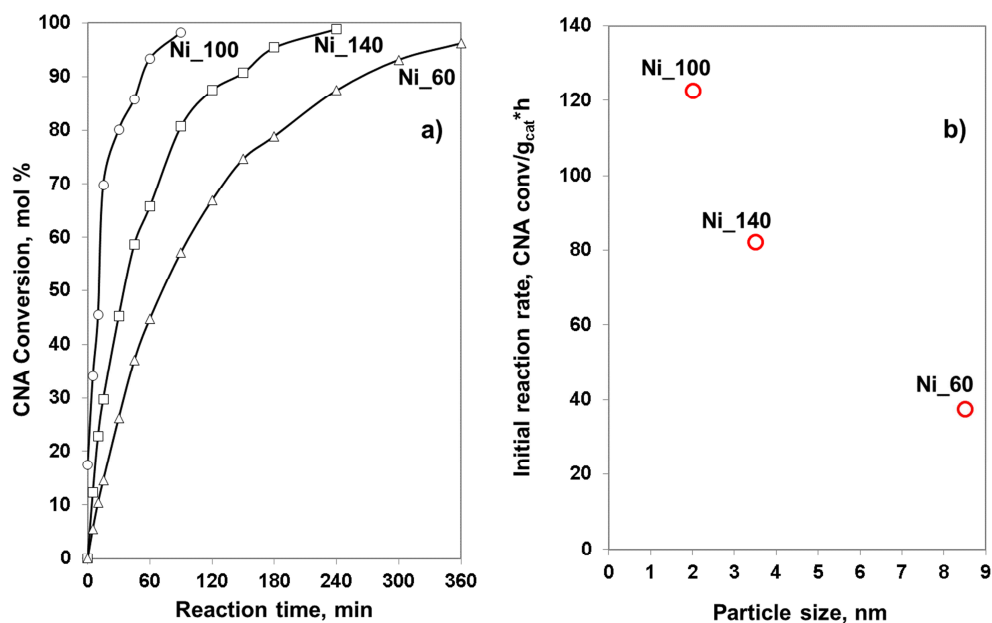


**Figure 10.** CNA conversion evolution with reaction time (a), and the initial conversion rate as a function of the initial NiO NPs size (for Ni<sub>100</sub> and Ni<sub>140</sub> from TEM; for Ni<sub>60</sub> from average crystallite size from XRD (b) for the MI-derived materials. Reaction conditions: 1 mL CNA, 0.133 g catalyst, 40 mL isopropanol,  $P(H_2) = 10$  bar,  $T = 60$  °C, stirring rate = 750 rpm.

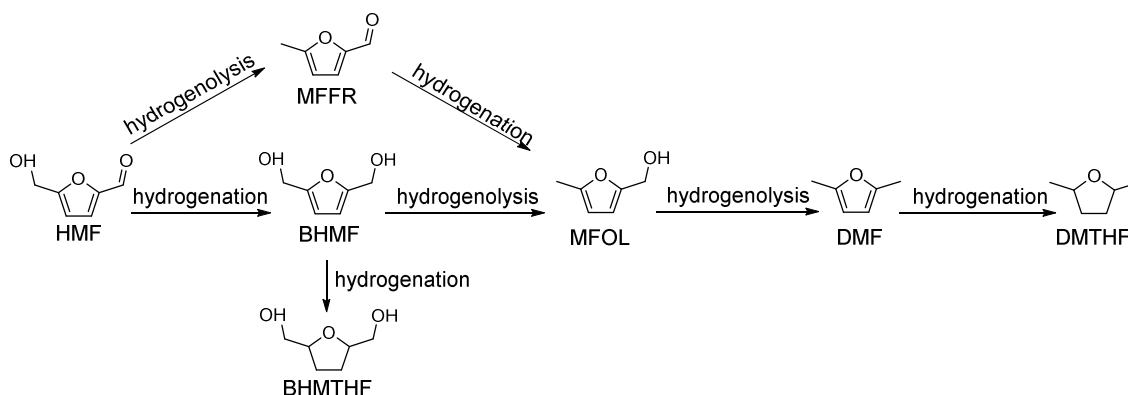
MI-derived Ni catalysts were first tested in the liquid-phase hydrogenation of cinnamaldehyde, under mild reaction conditions of temperature. Cinnamaldehyde (CNA) is an  $\alpha,\beta$ -unsaturated aldehyde, which generally can produce various products issued by hydrogenation of both C=C and C=O groups.

Over Ni-based catalysts, only hydrocinnamaldehyde (HCNA, by C=C bond hydrogenation) and hydrocinnamyl alcohol (HCNOL, by hydrogenation of HCNA) are expected to form, with a selectivity towards HCNA higher than 80 % at all conversion levels [25]. Therefore, the hydrogenation of CNA is proposed here as a model reaction for the evaluation of the catalytic properties of solids, thus allowing a pertinent assessment of the samples only in accord with their catalytic activity. The evolutions of the conversion of CNA with reaction time, obtained for Ni\_60, Ni\_100 and Ni\_140 catalysts, are presented in Fig. 10a. For Ni\_60 (large particle size - Figure 6), the complete CNA conversion is not achieved in 360 min, and a hydrogenation initial rate of  $37.47 \text{ mmolCNA.g}_{\text{cata.}}^{-1}.\text{h}^{-1}$  is measured (Figure 10). Ni\_140 sample shows a nearly complete CNA conversion after 240 min and an initial reaction rate of  $82.18 \text{ mmolCNA.g}_{\text{cata.}}^{-1}.\text{h}^{-1}$ . When small Ni NPs are highly dispersed on the silica support (Ni\_100), the complete CNA conversion is obtained in 90 min, with an initial reaction rate of  $122.76 \text{ mmolCNA.g}_{\text{cata.}}^{-1}.\text{h}^{-1}$ , which is the maximum reaction rate in the series. Thus, Ni\_100 shows superior catalytic activity, which is about 1.5 times higher than that of Ni\_140 and 3 times higher than Ni\_60. In Figure 10b, it can be observed that the initial reaction rate well - correlates with the NPs size for the MI-derived catalyst. The results highlight the improvement of catalytic activity of Ni/SBA-15 catalysts with the decrease in the NPs size. These results are explained by the specific localization of small NPs (confined in mesopores or micropores), the high dispersion of the metallic Ni NPs in the case of Ni\_100, this material exposing consequently the highest fraction of active Ni atoms able to activate and transform CNA molecules by reaction with the molecular hydrogen. For Ni\_140, where the NPs size increases up to 3.5 nm, the difference in activity is clearly observed in terms of decreased conversion.

Given the outstanding performance of Ni catalysts developed herein in CNA transformation, exploration of the efficiency of these MI-derived materials in the reductive conversion of another important biomass-based platform chemical (*i.e.*, HMF) was also performed. It has been well-established that the partial hydrogenation of HMF leads to the formation of BHMF (2,5-*bis*(hydroxymethyl)furan) while the full hydrogenation gives BHMTFH (2,5-*bis*(hydroxymethyl)tetrahydrofuran), as shown in Scheme 1, both of which are value-added

chemicals serving as polymer precursors and solvents [44,45]. The formation of BHMTHF involves the reduction of the furan ring, which generally requires relatively high hydrogenation activity of the catalyst [46]. The hydrogenolysis of the pendant groups leads to a valuable biofuel - DMF (2,5 - dimethylfuran) [47].

The conversions and product distributions obtained over Ni<sub>60</sub>, Ni<sub>100</sub> and Ni<sub>140</sub> catalysts are reported in Figure 11. Among the three MI-derived catalysts, Ni<sub>60</sub> exhibits relatively limited hydrogenation ability in HMF transformation, primarily catalyzing only the partial hydrogenation of HMF to BHMF (54 % yield) and giving a HMF conversion of 87 %. Ni<sub>140</sub> with a better dispersion of Ni NPs leads to an increase of HMF conversion up to 95 % though the partial hydrogenation reaction still dominates (64 % yield), indicating a higher hydrogenation activity than that of Ni<sub>60</sub>. For Ni<sub>100</sub> bearing highly dispersed Ni NPs, a nearly complete conversion of HMF (98.5 %) is obtained with a combination yield of BHMF and BHMTHF of 75 %. The heavily induced full hydrogenation of HMF over Ni<sub>100</sub> results in the formation of BHMTHF as the main product, indicating the high hydrogenation activity of this catalyst. Notably, a large quantity of DMF (17 % yield) is also formed over Ni<sub>100</sub>, suggesting some hydrogenolysis ability of this catalyst. These results confirm the efficiency of the IWP-confined Ni NPs to reach high hydrogenation activities, and at the same time, indicate the good potential of the application of the well-dispersed Ni<sub>100</sub> and Ni<sub>140</sub> for the production of valuable BHMF and BHMTHF from HMF.



**Scheme 1.** Reaction pathway for the transformation of HMF to some of the targeted compounds in the literature. HMF: 5-hydroxymethylfurfural; BHMF: 2,5-bis(hydroxymethyl)furan; BHMTHF:

2,5-*bis*(hydroxymethyl)tetrahydrofuran; MFFR: 5-methylfurfural; MFOL: 5-methylfurfuryl alcohol; DMF: 2,5 –dimethylfuran; DMTHF: 2,5-dimethyltetrahydrofuran.

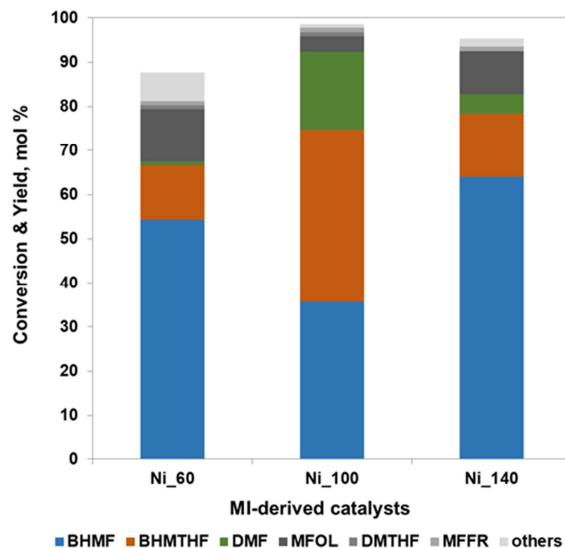


**Figure 11.** HMF conversion and the product distributions over the MI-derived materials. Reaction conditions: 0.03 g HMF, 21.1 mg catalyst, 1.5 mL *1,4*-dioxane,  $P(H_2) = 15$  bar,  $T = 130$  °C, reaction time = 1 h, stirring rate = 700 rpm.

## CONCLUSIONS

The second pore network of the SBA-15 host materials plays an important role in determining the Ni(O) NPs size and localization. The absence of the IWP connection between adjacent pores results in a worse diffusion of the precursor melt, thus forming large extra-porous aggregates. The size of the IWP and the presence of interconnected pores both facilitate the formation of pore-encapsulated and very small Ni(O) NPs, which can be of around 2 nm in size for Ni\_100. The catalytic activity of Ni MI-derived materials in the liquid-phase hydrogenation reaction of cinnamaldehyde is shown to significantly increase when the very small nickel particles are located in the silica intra-wall pores. Besides, the MI-derived catalysts with finely dispersed nickel particles show high potential in the reductive transformation of HMF to value-added BHMF and BHMTHF. This study provides new insights into how the microenvironment existing between the pore-occluded polymer and inorganic walls can be explored to stabilize highly dispersed M(O) NPs, *in fine*, to produce excellent catalysts for hydrogenation reactions.

## ACKNOWLEDGEMENTS

This work was partially supported by two grants of the Romanian National Authority for Scientific Research, CNCS-UEFISCDI (project numbers PN-II-RU-TE-2012-3-0403 and PN-II-ID-PCE- 2011-3-0868). Shuo CHEN acknowledges Chinese Scholarship Council for the support through the Ph.D. grant No.201505130002. Chevreul Institute (FR 2638), Ministère de l'Enseignement Supérieur et de la Recherche et de l'Innovation, Région Hauts-de-France and FEDER are acknowledged for supporting and funding partially this work.

## REFERENCES

- [1] P. Mäki-Arvela, J. Hájek, T. Salmi, D.Y. Murzin, *Appl. Catal. A: Gen.* 292 (2005) 1-49.
- [2] Z. Bian, S. Das, M. H. Wai, P. Hongmanorom, S. Kawi, *ChemPhysChem* 18(22) (2017) 3117-3134.
- [3] H. Tian, X. Li, L. Zeng, J. Gong, *ACS Catal.* 5 (2015) 4959-4977.
- [4] S. Singh, R. Kumar, H. D. Setiabudi, S. Nandac, D.-V. N. Vo, *Appl. Catal. A: Gen.* 559 (2018) 56-74.
- [5] T.W. Hansen, A.T. Delariva, S.R. Challa, A.K. Datye, *Acc. Chem. Res.* 46 (2013) 1720-1730
- [6] P. Munnik, P.E. de Jongh, K.P. de Jong, *Chem. Rev.* 115 (2015) 6687-6718.
- [7] J.R.A. Sietsma, J.D. Meeldijk, M. Versluijs-Helder, A. Broersma, A.J. van Dillen, P.E. de Jongh, K.P. de Jong, *Chem. Mater.* 20 (2008) 2921-2931.
- [8] G. Prieto, J. Zečević, H. Friedrich, K. P. de Jong, P.E. de Jongh, *Nat. Mater.* 12 (2013) 34-39.
- [9] U. Ciesla, F. Schuth, *Microporous Mesoporous Mater.* 27 (1999) 131-149.
- [10] A. Taguchi, F. Schuth, *Microporous Mesoporous Mater.* 77 (2005) 1-45.
- [11] F. Schurh, A. Wingen, J. Sauer, *Microporous Mesoporous Mater.* 44-45 (2001) 465-476.
- [12] L.H. Wee, M. Meledina, S. Turner, K. Custers, S. Kerkhofs, G. van Tendeloo, J. A. Martens, J. *Mater. Chem. A* 3 (2015) 19884-19891.

- [13] L.H. Wee, M. Meledina, S. Turner, K. Custers, S. Kerkhofs, S.P. Sree, E. Gobechiya, C.E.A. Kirschhock, G. Van Tendeloo, J. A. Martens, RSC Adv. (2016) 46678-46685.
- [14] A. Ungureanu, B. Dragoi, A. Chiriac, S. Royer, D. Duprez, E. Dumitriu, J. Mater. Chem. 21 (2011) 12529- 12541.
- [15] C. Ciotonea, B. Dragoi, A Ungureanu, A. Chiriac, S. Petit, S. Royer, E. Dumitriu, Chem. Commun. 49 (2013) 7665-7667.
- [16] Y. Park, T. Kang, P. Kim, J. Yi, J. Colloid Interface Sci. 295 (2006) 464-471.
- [17] A. Ungureanu, B. Dragoi, A. Chiriac, C. Ciotonea, S. Royer, D. Duprez, A.S. Mamede, E. Dumitriu, ACS Appl. Mater. Interfaces 5 (2013) 3010-3025.
- [18] Y.M. Wang, Z.Y. Wu, J.H. Zhu, J Solid State Chem. 177 (2004) 3815-3823.
- [19] Y.M. Wang, Z.Y. Wu, H.J. Wang, J.H. Zhu, Adv. Funct. Mater. 16 (2006) 2374-386.
- [20] W.H. Tian, L.B. Sun, X.L. Song, X.Q. Liu, Y. Yon, Langmuir 26 (2010) 17398-17404.
- [21] C.F. Zhou, Y.M. Wang, Y. Cao, T.T. Zhuang, W. Huang, Y.A. Chun, J.H. Zhu, J. Mater. Chem. 16 (2006) 1520-1528.
- [22] J.K. Shon, S.S. Kong, Y.S. Kim, J.H. Lee, W.K. Park, S.C. Park, J.M. Kim, Microporous Mesoporous Mater. 120 (2009) 441-446.
- [23] M.B. Zheng, J. Cao, S.T. Liao, J.S. Liu, H.Q. Chen, Y. Zhao, W.J. Dai, G.B. Ji, J.M. Cao, J. Tao, J. Phys. Chem. C 113 (2009) 3887-3894.
- [24] K. Jian, T.C. Truong, W.P. Hoffman, R.H. Hurt, Microporous Mesoporous Mater. 108 (2008) 143-151.
- [25] C. Ciotonea, B. Dragoi, A. Ungureanu, C. Catrinescu, S. Petit, H. Alamdari, E. Marceau, E. Dumitriu, S. Royer, Catal. Sci. Technol. 7 (2017) 5448-5456.
- [26] C. Ciotonea, I. Mazilu, B. Dragoi, C. Catrinescu, E. Dumitriu, A. Ungureanu, H. Alamdari, S. Petit, S. Royer, ChemNanoMat. 3 (2017) 214-222.
- [27] Q Zhang, T. Zhang, Y. Shi, B. Zhao, M. Wang, Q. Liu, J. Wang, K. Long, Y. Duan, P. Ning, Journal CO<sub>2</sub> Utilization 17 (2017) 10-19.

- [28] X. Ning, Y. Lu, H. Fu, H. Wan, Z. Xu, S. Zheng, *ACS Appl. Mater. Interfaces* 9 (2017) 19335-19344.
- [29] P.E. de Jongh, T.M. Eggenhuisen, *Adv. Mater.* 25 (2013) 6672-6690.
- [30] W. Yue, W. Zhou, *Chem. Mater.* 19 (2007) 2359-2363.
- [31] Q. Jiang, Z.Y. Wu, Y.M. Wang, Y. Cao, C.F. Zhou, J.H. Zhu, *J. Mater. Chem.* 16 (2006) 1536-1542.
- [32] T.M. Eggenhuisen, J.P. den Breejen, D. Verdoes, P.E. de Jongh, K.P. de Jong, *J. Am. Chem. Soc.* 132 (2010) 18318- 8325.
- [33] A. Galarneau, H. Cambon, F. Di Renzo, R. Ryoo, M. Choi, F. Fajula, *New J. Chem.* 27 (2003) 73-79.
- [34] F. Kleitz, F. Bérubé, R. Guillet-Nicolas, C. M. Yang, M. Thommes, *J. Phys. Chem. C* 114 (2010) 9344-9355.
- [35] F. Bérubé, A. Khadraoui, M. T. Janicke, F. Kleitz, S. Kaliaguine, *Ind. Eng. Chem. Res.* 49 (2010) 6977-6985.
- [36] F. Bérubé, A. Khadraoui, J. Florek, S. Kaliaguine, F. Kleitz, *J. Colloid Interface Sci.* 449 (2015) 102-114.
- [37] D. Zhao, J. Feng, N. Huo, G. Melosh, H. Fredrickson, B. F. Chmelka, G. D. Stucky, *Science* 279 (1998) 548-552.
- [38] L. Cao, T. Man, M. Kruk, *Chem. Mater.* 21(6) (2009) 1144-1153.
- [39] V.T. Hoang, Q. Huang, M. Eic, T.O. Do, S. Kaliaguine, Effect of the intrawall microporosity on the diffusion characterization of bi-porous SBA-15 materials, in W.C., Conner J. Fraissard (Eds.), *Fluid Transport in Nanoporous Materials*, Springer, Netherlands, 2006, pp. 591-602.
- [40] C.J. Rasmussen, A. Vishnyakov, M. Thommes, B.M. Smarsly, F. Kleitz, A.V. Neimark, *Langmuir* 26 (2010) 10147-10157.
- [41] C. He, Q. Li, P. Li, Y. Wang, X. Zhang, J. Cheng, Z. Hao, *J Chem. Engineer.* 162 (2010) 901-909.

- [42] G. Wanka, H. Hoffmann, W. Ulbricht, *Macromolecules* 27 (1994) 4145-4159.
- [43] A.B.R. Mayer, *Polym. Adv. Technol.* 12 (2001) 96-105.
- [44] D. Scholz, C. Aellig, I. Hermans. *ChemSusChem.* 7 (2014) 268-275.
- [45] L. Hu, L. Lin, Z. Wu, S. Y. Zhou, S. J. Liu. *Renew. Sustain. Energy Rev.* 74 (2017) 230-257.
- [46] X. Tang, J. Wei, N. Ding, Y. Sun, X. Zeng, L. Hu, S. Liu, T. Lei, L. Lin. *Renew. Sustain. Energy Rev.* 77 (2017) 287-296.
- [47] Y. Qian, L. Zhu, Y. Wang, X. Lu. *Renew. Sustain. Energy Rev.* 41 (2015) 633-646.

# Metal Infiltration

Selective localization of NPs within intra-trail pores

